A Water Fraction Measurement Method Using Heuristic-Algorithm-Based Electrical Capacitance Tomography Images Post-Processing Technology

BO LIU[1], CHENHUI TANG[2], KAIHAO TANG[3], AND HONGLI HU[3], (Member, IEEE)
[1]School of Mechatronic Engineering, Xi'an Technological University, Xi'an 710021, China
[2]State Grid Sichuan Electric Power Company Maintenance Company, Chengdu 610041, China
[3]State Key Laboratory of Electrical Insulation and Power Equipment, School of Electrical Engineering, Xi'an Jiaotong University, Xi'an 710049, China

Corresponding author: Kaihao Tang (mrerr07@stu.xjtu.edu.cn)

ABSTRACT This paper presents a sectional water fraction measurement method using electrical capacitance tomography (ECT) image. To achieve a desired measurement accuracy, an optimal threshold-search method based on fast simulated annealing (FSA) algorithm is applied for image binarization; and to guarantee the imaging time consumption, fast fixed point continuation (FFPC) iterative algorithm cooperating with the compressed sensing (CS) theory was applied to the image reconstruction. In this study, the imaging time consumption and the measurement accuracy of water fraction are used to compare the proposed method and other methods. A numerical model is established with COMSOL Multiphysics to conduct the simulative validation of the proposed method firstly and physical experiments are conducted then. The experiment results show the average relative error of water fraction is lower than 15%, where the even as low as 3.68%.

INDEX TERMS Electrical capacitance tomography, fast simulated annealing, image binarization, compressed sensing, water fraction measurement.

I. INTRODUCTION

Electrical capacitance tomography (ECT) has been widely applied to multiphase flow phase fraction detection in various industrial areas such as chemical engineering, natural gas transportation, and electric power plant [1]. For some industrial processes (e.g. natural gas mining and transportation), gas-water two phase flow plays a crucial role and the water fraction measurement for it has far-reaching impact in the conveying system.

There are currently many studies trying to realize this application of ECT. Dong et al put forward a method based on ERT (mathematically similar to ECT) to extract cross-correlation eigenvalue of void fraction and the measured values [2]. Yu [3] applied ERT image to voidage measurement for gas-liquid two-phase flow, using modified BFGS and Otsu algorithms for image reconstruction and binarization, respectively. Wangjiraniran *et al.* [4] investigated the effect of deviation of signal obtained from each adjacent measuring plane

The associate editor coordinating the review of this manuscript and approving it for publication was Wen Chen.

of intrusive WMT on void fraction measurement. Wang [5] proposed a new method based on ECT for voidage measurement of gas-oil two phase flow, and the image reconstruction algorithm is sample back projection. Based on ECT and LS-SVM, Li *et al.* [6] put forward a new method for voidage of gas-oil flow without imaging process. In 2018, Moreira da Mota *et al.* [7] proposed a modified method ECTM (based on ECT theory) to realize water fraction measurement. This method simplifies the 12-electrode sensor into a 2-electrode sensor, and uses rotation measurement to obtain 12 capacitance values for water fraction measurement.

Generally, calculating the water fraction from an ECT image is a kind of image gray operation. According to Multiphase fluid dynamics, the water fraction of gas-water two-phase flow can be defined as

$$\alpha = \frac{A_{\mathrm{w}}}{A_{\mathrm{w}} + A_{\mathrm{g}}} \qquad (1)$$

where A_{w} is sectional area of water phase, A_{g} is cross-sectional area of gas phase, *a* is value of water fraction. Once the image (i.e. the phase distribution) of a certain section is

B. Liu *et al.*: Water Fraction Measurement Method Using Heuristic-Algorithm-Based ECT Images Post-Processing Technology

IEEE *Access*

obtained, the water fraction can be calculated from image gray, expressed as

$$\alpha = \frac{1}{M} \sum_{i=0}^{M} f_i \qquad (2)$$

In (2), f_i is the gray value (regulated to [0,1]) of the i-th pixel, where 1 stands for water phase, and 0 stands for gas phase; M is the total number of pixels of sectional tube. It can be seen from (2) that the performance of the ECT image-based water fraction measurement is limited by the quality of the reconstructed images; a sharped and deblurred image is desired for such application. Moreover, to meet the requirement in real-time, the fast-converging property of the applied image reconstruction algorithm is necessary.

The reconstructed image of ECT contains a number of pixels far more than the measured capacitances of ECT sensor, therefore the inverse problem of ECT is ill-posed [8]. All the algorithms mentioned above are sensitivity-based, so the ill-posed nature is hard to overcome. Thus, some researchers turn to find a new method which does not rely on the sensitivity matrix. Wang et al developed an AST-ELM method [9] which directly establishes the map between measured capacitances and images. This neural network based algorithm does not need a sensitivity matrix compared with traditional algorithms (such as the Landweber iterative and the linear back projection algorithm), so the ill-posed nature of ECT's inverse system can be solved. However, the neural network based algorithm requires a large training set which is unfeasible in some occasions.

The existing algorithms have different limitations. The compressed sensing (CS) theory was proposed by Donoho in 2006, using the sparseness or compressibility of the original signal to reconstruct the original signal with only a small amount of sampling [10]. In ECT applications, Xia *et al.* [11] proposed an image reconstruction method based on CS theory called fast linearized alternating direction method of multipliers (FLADMM), and compared it with the linear back projection (LBP) algorithm, the Landweber iteration algorithm (LIA), and the conjugate gradient (CG) method. Zhang *et al.* [12] applied the CS theory based on gradient projection for reconstruction algorithm to solve inverse-problem of ECT, and draw a conclusion that the CS-based image reconstruction algorithm can improve the image quality and reduce the time consumption.

In this study, a fast fixed point continuation (FFPC) iterative algorithm based on CS was applied to ECT image reconstruction, with the assistance of optimal threshold-search method based on fast simulated annealing (FSA) heuristic algorithm to binary images for water fraction measurement on gas-water two phase flow. This stratagem can not only inherit the merits of CS-based reconstruction algorithm, but also further make the reconstructed image suitable for water fraction calculation.

This study firstly introduces the fundamental of the proposed CS-based image reconstruction algorithm and the FSA

binarization algorithm. Simulative and experimental validation are carried out then, with the results of the proposed method and other traditional methods compared.

II. IMAGING ALGORITHM AND ECT SYSTEM
A. BRIEF INTRODUCTION OF COMPRESSED SENSING THEORY AND ITS APPLICATION IN ECT
According to compressing sensing theory, k-sparse signal means N dimensional signal $x \in \mathbf{R}^N$ has at most k non-zero elements, i.e. $\| x \|_0 \le k$. Another case, x can be converted by sparse domain Ψ, i.e. $x = \Psi z$. As a result, a sparse signal z is got, and $\| z \|_0 \le \mathbf{k}$ [13].

Now supposing $[\Psi_1, \Psi_2, \ldots, \Psi_N]$ is an orthogonal basis vector in $\mathbf{R}^N$, then any $N \times 1$ dimensional discrete signal in domain $\mathbf{R}^N$ can be linear expressed as

$$x = \sum_{i=1}^{N} \Psi_i z_i = \Psi z \qquad (3)$$

In (3), $\Psi = [\Psi_1, \Psi_2, \cdots, \Psi_N]$ is an $N \times N$ dimensional sparse basis matrix, z is the sparse vector converted from x by Ψ. If only a few elements in z have large values but most of them have small values, and original signal x can be recovered by z, that is to say, x is compressible.

Then supposing an $M \times N$ dimensional ($M \ll N$) matrix Φ, called ''observation set'' [14], then use to sample the $M \times 1$ dimensional signal of x, equation as follow

$$y = \Phi x = \Phi \Psi z \qquad (4)$$

where y is the observation vector converted by x. Let $\mathbf{A} = \Phi \Psi$, then (4) can be simplified as

$$y = \mathbf{A} z \qquad (5)$$

where $\mathbf{A}$ is called the probing matrix. The observation vector y obtained by detection.

The most direct approach to calculate sparse vector z is transforming (5) into an l_0-norm constraint optimization problem. But this is an NP-hard problem [15], hard to be solved. However, (5) can be changed into an l_1-norm constraint optimization problem [16], presented as

$$\begin{cases} z_{\text{opt}} = \arg \min_{z \in R^N} \|z\|_1 \text{ s.t. } \mathbf{A}z = y \\ x_{\text{opt}} = \Psi z_{\text{opt}} \end{cases} \qquad (6)$$

There are three major approaches to solve (6): interior point method (IPM), gradient projection for sparse Reconstruction (GPSR), and fixed point continuation (FPC) [17]. But for solving large-scale problems, the above three traditional iterative methods are limited by their slow convergence rate.

Improved from FPC, fast fixed point continuation (FFPC) [18] algorithm makes higher the peak signal to noise ratio of image reconstruction and lower the relative errors. Furthermore, it reduces running time when the sampling rate is low.

Once FFPC is used to solve optimization problem (6), (6) can be transformed into the following iterative formula

$$z^{n+1} = \text{sgn}(z^n - \tau \nabla f(z^n)) \odot \max \{|z - \tau \nabla f(z)| - \tau \mu, 0\}$$

$$\qquad (7)$$

where μ is the contraction factor in [0,1], and τ is the regularization parameter. $\tau\mu$ effects the iterative convergence of (7), higher the value, faster the convergence speed. In this study, μ is determined to be 1. The expression of $f(z)$ in (7) is

$$f(z) = \frac{1}{2}\|\mathbf{A}z - y\|_2^2 \qquad (8)$$

To accelerate the convergence of (7), reference [18] indicated that Barzilai and Borwein Gradient method [19], [20] can be used for the updating of parameter τ in the k-th iteration

$$\tau^k = \frac{\|z^k - z^{k-1}\|^2}{(z^k - z^{k-1})^{\mathrm{T}}(\nabla f(z^k) - \nabla f(z^{k-1}))} \qquad (9)$$

The initial value of τ (i.e. τ^0) can be determined by

$$\tau^0 = \alpha \cdot \max(\mathbf{A}^{\mathrm{T}}y) \qquad (10)$$

where α is a positive constant that makes τ^0 a relatively large number. In this paper, we adopt $\alpha = 1$. Equations (7)-(10) have illustrated the iteration of FFPC algorithm in detail.

To apply the CS theory in ECT, the gray vector g of image to be constructed is the original signal x in CS as discussed above. In this study, discrete Fourier transform (DFT) basis is used as sparse domain Ψ_{DFT} to make g sparse for satisfying the premise of CS theory firstly, to get sparse expression

$$g = \Psi_{\mathrm{DFT}}z \qquad (11)$$

Substituting (11) into the linear model of ECT system

$$c_{\mathrm{m}} = \mathbf{S}g \qquad (12)$$

and the linear model expressed as (12) based on CS theory can be transformed into

$$c_{\mathrm{m}} = \mathbf{S}\Psi_{\mathrm{DFT}}z \qquad (13)$$

In (12) and (13), c_{m} is the $M\times 1$ dimensional vector of normalized capacitance measurement, functioning as the observation vector. $\mathbf{S}$ is the $M \times N$ dimensional sensitivity matrix, functioning as the observation matrix of CS. $N \times N$ dimensional matrix Ψ_{DFT} is the sparse domain and $N \times 1$ dimensional vector z is the sparse signal vector of original signal vector g. $\mathbf{A} = \mathbf{S}\Psi_{\mathrm{DFT}}$ is the probing matrix.

As Candes proposed before [17], probing matrix $\mathbf{A}$ satisfy the restricted isometry property (RIP) condition if sparse basis matrix Ψ_{DFT} and observation matrix $\mathbf{S}$ are not related. Reference [21] proved that a Gaussian random matrix is irrelevant with the sparse basis Ψ_{DFT}. Therefore, if a Gaussian random matrix is chosen as observation matrix, the sensing matrix can meet the RIP. Following this idea, we must rearrange the rows of the sensitivity matrix with a Gaussian random vector; the length of the Gaussian random vector is the same as the number of $\mathbf{S}$'s row, and each element of the random vector indicates the new row index for $\mathbf{S}$. Therefore, such rearrangement of $\mathbf{S}$ (denoted as $\mathbf{S}_{\mathrm{new}}$) becomes the applied observation matrix in this paper, which approximately satisfy the RIP condition (according to Ref. [23]). Obviously, the rearrangement of $\mathbf{S}$ is still the sensitivity

matrix of ECT. The same rearrangement is conducted to the capacitance vector cm. Since, the inverse problem of ECT based on the CS theory can be written as

$$\begin{cases} z_{\mathrm{opt}} = \arg \min_{z \in R^N} \|z\|_0 & \text{s.t. } c_{\mathrm{new}} = \mathbf{S}_{\mathrm{new}}\Psi_{\mathrm{DFT}}z \\ g_{\mathrm{opt}} = \Psi_{\mathrm{DFT}}z_{\mathrm{opt}} \end{cases} \qquad (14)$$

where c_{new} is the Gaussian rearrangement for c_{m}. Equations (14) is a classical minimum l_0 norm problem, can be solved by FFPC iterative algorithm mentioned above.

In brief, the whole process of ECT inverse problem solving based on CS and FFPC is: 1) solve the sparse vector z_{opt} in (14) by FFPC (as described in (7)-(10)); 2) calculate the gray vector g_{opt} by according to (11).

B. OPTIMAL THRESHOLD SEARCHING METHOD BASED ON FSA

The main purpose of the optimal threshold searching is to find an optimized threshold for a reconstructed gray vector g, and binarize g accordingly; the artifact can be removed and the areas (where medium exists) of small gray value can be enhanced. Such binary image (gray vector) are suitable for water fraction calculation by formula (2).

To globally search the optimal threshold th ($0 < th < 1$), the optimal threshold searching can be turned into an optimization problem that search a threshold for g, which minimize the capacitance residual δ. This optimization problem and the definition of δ are written as

$$\begin{cases} g_{\mathrm{opt}}^{th} = \arg \min_{g \in \mathbf{R}^N} \|\delta\|_2^2 \\ \delta = \mathbf{S}P_{th}(g) - c_{\mathrm{m}} \end{cases} \qquad (15)$$

In (15), g_{opt}^{th} is the binary gray vector of g (binarized by the optimal threshold th); $P_{th}(\cdot)$ is the threshold operator, making the elements of g one if those are equal or greater than th, and zero if those are less than th. c_m and $\mathbf{S}$ are the normalized measurement vector and the sensitivity matrix of ECT.

To rapidly solve the optimization problem of (15), the fast simulated annealing (FSA) algorithm is employed. Improved from the simulated annealing (SA) algorithm, FSA has a faster convergence speed. FSA is a kind of heuristic algorithms, inspired by thermodynamics. It explores the entire surface of the function and tries to optimize the function as it moves uphill and downhill. Other than gradient algorithms, it is independent of the starting value, and able to deviate from local optimal values, continuing to find global optimal values.

And compared with other typical heuristic algorithms, such as the particle swarm optimization (PSO) and the genetic algorithm (GA), FSA consumes less time to find a global optimal solution. The next, FSA and its application in optimal threshold searching problem is to be briefly introduced.

According to [22], when use FSA to search a vector x minimizing the objective function $f(x)$, firstly, the start

B. Liu *et al.*: Water Fraction Measurement Method Using Heuristic-Algorithm-Based ECT Images Post-Processing Technology

IEEE*Access*

temperature T_0, needs to be initialized, and the initial energy E_0 can be set as $f(x_0)$. Then, set the step length of each iteration v. Both x and v are vectors of $n \times 1$. The updating formula for x

$$x_i = x_{i-1} + rv \qquad (16)$$

where r is a random obeying standard uniform distribution in $[-1, 1]$, and i is number of iteration.

In every step, a new energy E_i is calculated by $f(x_i)$. If E_i is lower than E_{i-1}, E_i is accepted as current energy, and the algorithm goes downhill; if E_i is the lowest current energy, save x_i as current best value of optimization.

If E_i is greater than or equal to E_{i-1}, a criteria motivated by thermodynamics (called "Metropolis criteria") decides acceptance or not, if the value of

$$p = \exp\left(\frac{E_c - E_i}{T_0}\right) \qquad (17)$$

is larger than p_r (which is a uniformly distributed random number in $[0, 1]$), E_i is accepted as current energy, and the algorithm goes uphill; otherwise, E_i is rejected. Obviously, the higher energy is, the more probability to accept E_i and go uphill.

As for conventional simulated annealing (SA), the iteration of the temperature follows

$$T_i = T_0 / \log(1 + i) \qquad (18)$$

The temperature declining schedule shown as (18) is too slow to practise [23]. Instead, FSA uses another iteration schedule expressed as (19)

$$T_i = T_0 / (1 + i) \qquad (19)$$

It is much faster than the conventional method (SA) to utilize expression (19) to set down temperature.

The algorithm ends by comparing the last minimum energy with the energy of each annealing step, until the iteration end temperature; if all these difference less than a certain positive number ε, iteration terminates.

When FSA is applied to the optimization problem (15), optimal threshold value g_{opt} is the target vector x, and the step length is set up as 10^{-10} for higher accuracy. Initial temperature T_0 is $90\,^{\circ}\text{C}$ and end value is $10\,^{\circ}\text{C}$. The annealing repeats 1000 times. The energy expression is

$$E = \left\| Sg^{\text{th}} - c_{\text{m}} \right\|_2^2 \qquad (20)$$

And the iteration steps in each temperature cooling process can be described as:

step1: $x_i^{\text{th}} = x_{i-1}^{\text{th}} + r \cdot 10^{-10}$;

step2: if $g_i^n > x_i^n \ g_i^n = 1$,

   else $g_i^n = 0$;

step3: $E_i = \| S \cdot g_i^{\text{th}} - c_{\text{m}} \|_2^2$;

step4: if $E_i < E_{i-1} E_c = E_i$,

   else if $p > p_r E_c = E_i$,

   else $i = i+1$; $i = 1, 2, \ldots, 1000$

TABLE 1. Units for magnetic properties.

Parameter Description	Value
Inner radius of the pipe wall	23 mm
Outer radius of the pipe wall	25 mm
Relative permittivity of the pipe wall	3.7
Length of sensing electrode	125 mm
Cover angle of sensing electrode	26°
Spacing angle between adjacent electrodes	4°
Radius of the grounded screen	35 mm

where $x_i^{\text{th}} = [x_i^1, x_i^2, \ldots, x_i^n]$ is the threshold vector, and $g_i^{\text{th}} = [g_i^1, g_i^2, \ldots, g_i^n]$ is the threshold gray vector. n is the vector length. p is the Metropolis criteria mentioned before. Steps 1-4 are a single loop (called annealing) of FSA iteration. Repetitively execute the 4 steps until the end temperature reached.

In summary, optimal threshold searching method based on FSA contains three parts [23]: 1) generate the states are with a standard uniform distribution; 2) use the Metropolis criteria to allow occasional upward-climbing among decreasing; 3) artificially cool the temperature by (16) for faster and accurate convergence.

III. SIMULATION AND EXPERIMENT
A. INTRODUCTION OF THE DESIGNED ECT SYSTEM
In this study, we design an ECT system for experimental validation. The designed ECT system is presented in Fig. 1. This system is consisted of a 12-electrode ECT sensor, a capacitance measurement circuit, and an upper computer (a PC). Geometry parameters of the designed 12-electrode ECT sensor are listed in Table 1. The sensing electrodes are mounted outside the 2mm-thickness acrylic insulation pipe, and a grounded outer screen is used for preventing interference of ambient noise (Fig. 1(b)).
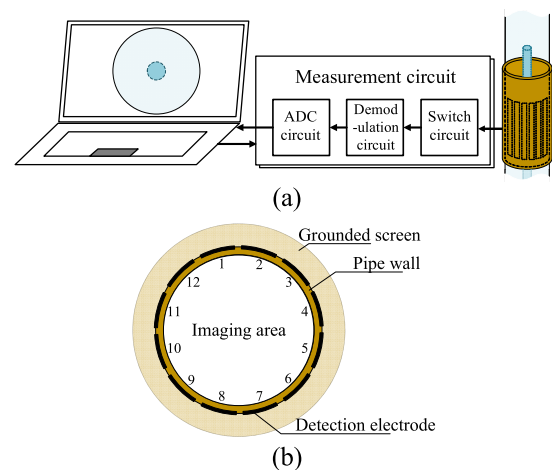

(a)

(b)

FIGURE 1. The designed ECT system. (a) ECT system; (b) cross-sectional view of 12-electrodes ECT sensors.

The measurement circuit is designed following AC capacitance measurement principle [24], whose capacitance resolution is less than 0.01 pF. The whole system for experiments is shown in Fig. 1(a).

IEEE *Access*

B. Liu *et al.*: Water Fraction Measurement Method Using Heuristic-Algorithm-Based ECT Images Post-Processing Technology

The PC in this system has a CPU in 3.20 GHz (Intel® Core™ i7-8700) and two channels of 8 GB RAMs. In the next of this paper, the image reconstruction algorithms, the image binarization algorithms, and the experiments are also tested on the same PC.

B. SIMULATIVE ANALYSIS

The simulation model for the 12-electrode ECT sensor is established with COMSOL Multiphysics, following the parameters shown in Table 1. The geometry model established is presented in Fig. 2. In this simulation section, we set 5 different medium distributions (shown in the first column of Fig. 3) to simulate different flow regimes.
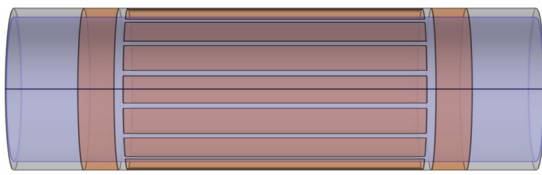
FIGURE 2. The 12-electrodes sensor model for simulation.

For the first three distributions, the water region is limited into several cylinder areas, simulating the gas-dominated situations. And the remaining two annular distributions represent water-dominated situations. The radius of each cylinder is 5.75 mm, taking up 6.25% of the sensor's cross section area, and the distance between the axes of the cylinder and the sensor is regulated to 15 mm. The thicknesses of the two annular mediums are 7 and 14 mm, taking up 57.47% and 81.10% of the cross section area.

The 5 different medium distributions are used to test the algorithms illustrated above. The simulated measured capacitances of the ECT sensor is obtained via the AC/DC module of COMSOL Multiphysics. Set the medium distribution alternatively, and the capacitances can be extracted after the corresponding numerical solving. And then, the simulated data can be used for the algorithm evaluation, with the aid of MATLAB.

1) COMPARISON BETWEEN LBP, LIA, AND CS-FFPC

The imaging area is divided into 2401 pixels. The proposed CS-FFPC image reconstruction algorithm is compared with linear back projection (LBP) algorithm and Landweber iterative algorithm (LIA) for each medium distribution. The reconstructed images are shown in Fig. 3. The iterations of LIA is 2500, and the initial regularization parameter τ of CS-FFPC algorithm is determined by (10).

It can be read from Fig. 3 that the boundary between phases is hardly to distinguish by LBP-reconstructed images; as for LIA, there is artifact in the reconstructed images and the boundary of water is blurred. However, the reconstructed images of CS-FFPC have clearer boundaries compared with LBP and LIA; the high-permittivity phase (water) can be identified easily from the images. It can be read from Fig. 3 that the water areas near to the center of the sensor
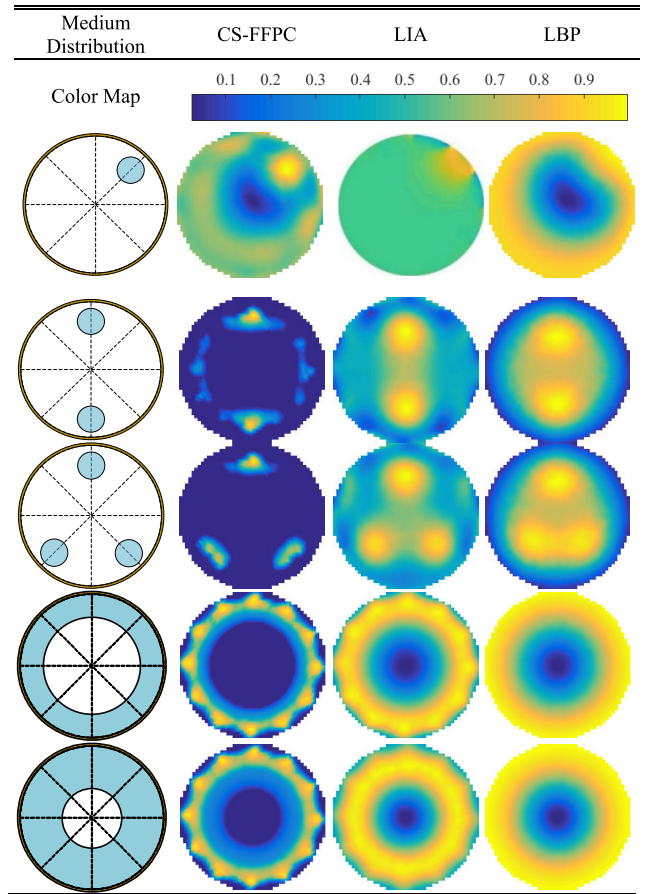
FIGURE 3. Images reconstructed by LBP, LIA, and CS-FFPC using simulated data.

are much bright than the areas at the edge. This is because the sensitivity of ECT has much smaller values at the center. Further, a widely used factor, image correlation coefficient (ICC) [25], is adopted to evaluate the quality of the three algorithms, which is defined as

$$\mathrm{ICC} = \frac{\sum_{i=1}^{n} (\hat{g}_i - \bar{\hat{g}})(g_i - \bar{g})}{\sqrt{\sum_{i=1}^{n} (\hat{g}_i - \bar{\hat{g}})^2 \sum_{i=1}^{n} (g_i - \bar{g})^2}} \times 100\% \quad (21)$$

where $\{\hat{g}_i\}$ and $\{g_i\}$ are the gray vectors the reconstructed image and the real image, respectively; $\bar{\hat{g}}$ and $\bar{g}$ are the mean value of elements in $\{\hat{g}_i\}$ and $\{g_i\}$, respectively. The higher the ICC is, the more precise the image reflects the real medium distribution.

The ICC calculated for the images presented in Fig. 3 is listed in Table 2.

As can be seen from Table 2, the ICC of CS-FFPC is much higher than that of both LBP and LIA, meaning the images reconstructed by CS-FFPC are more similar to the real object.

The average time consumptions of the three image reconstruction algorithms are listed in Table 3. It can be read from Table 3 that LBP has the minimum time consumption among the three, and LIA takes the most time to reconstruct an

B. Liu *et al.*: Water Fraction Measurement Method Using Heuristic-Algorithm-Based ECT Images Post-Processing Technology

IEEE *Access*

TABLE 2. The ICC of three reconstruction algorithms.

Medium Distribution	LBP (%)	LIA (%)	CS-FFPC (%)
1	32	64	72
2	48	66	78
3	41	56	74
4	56	71	77
5	62	73	82

TABLE 3. Average time consumption of LBP, LIA, and CS-FFPC.

Image Reconstruction Algorithm	Time Consumption (ms)
LBP	0.13
LIA	398.73
CS-FFPC	44.37

TABLE 4. The water fraction calculation based on ECT images.

Medium Distribution	Real (%)	PSO (%)	GA (%)	FSA (%)
1	6.25	12.82	23.26	5.76
2	12.50	11.52	13.48	12.07
3	18.75	22.76	28.25	20.43
4	51.61	56.58	58.55	56.47
5	84.68	76.34	76.88	77.85

image. As an iterative algorithm, CS-FFPC takes much less time compared with LIA, although it still needs much longer time than LBP. However, according to Fig. 3 and Table 2, CS-FFPC performance is the most desired (evaluated by the ICC and artifact).

To summarize, CS-FFPC is an algorithm guarantees both convergence speed and image quality, meeting the requirement of this study.

2) PERFORMANCE COMPARISON BETWEEN THREE HEURISTIC-ALGORITHM-BASED OPTIMAL THRESHOLD SEARCHING METHODS

To further process the reconstructed images, this part utilizes the optimal threshold searching method to binary reconstructed images. The performance of three optimal threshold searching methods based on the FSA, the Genetic Algorithm (GA), and the Particle Swarm Optimization (PSO) respectively are compared. The inertia factor for the SPO is 0.729; a 5-bit gene encoding is used for the GA; for FSA, the initial and the lowest temperature are set to 90°C and 10°C, respectively, and the number of annealing in each temperature is 1000. The results of the three image binarization algorithms are shown in Fig. 4.

As can be seen from Fig. 4, the binarization based on FSA performs better in approximating the distribution of high permittivity mediums than SPO and GA. To evaluate the performance of the three algorithms, the calculated water fraction (according to Eq. (2)) and the relative error (RE) of the measurement are listed in Table 4 and Table 5 respectively.

It is obvious (from Table 5) that the relative error of water fraction calculated by the FSA-based optimal threshold searching method is much lower than PSO and GA, which
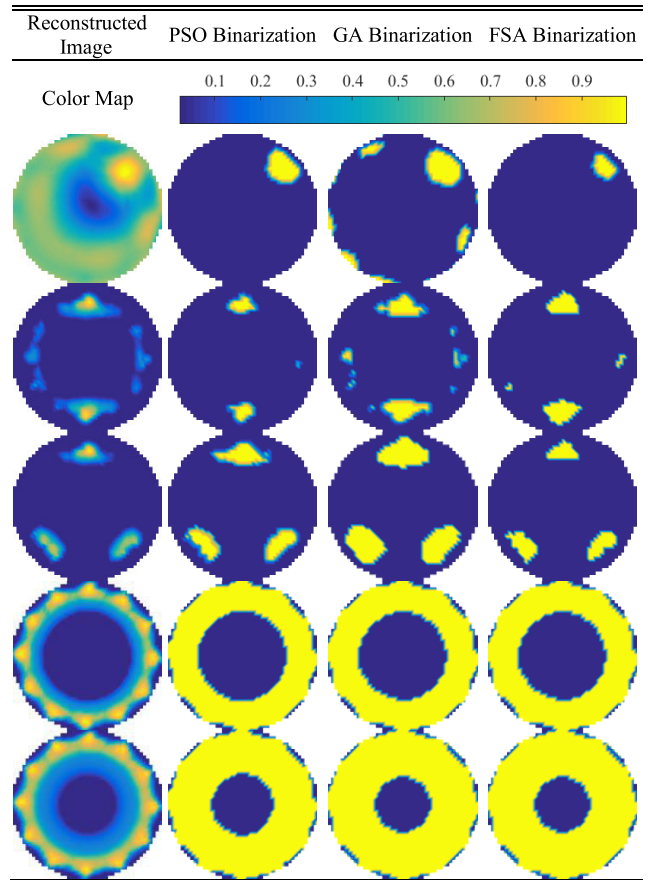

FIGURE 4. Images binarized by optimal threshold searching method based on FSA, GA, and SPO using simulated data.

TABLE 5. Relative error (RE) of water fraction calculation based on ECT images.

Medium Distribution	PSO (%)	GA (%)	FSA (%)
1	105.12	272.16	7.84
2	7.84	7.84	3.44
3	21.29	50.56	8.96
4	9.82	13.45	9.42
5	9.85	9.21	8.07

TABLE 6. Average time consumption of the image binarization algorithms based on PSO, GA, and FSA.

Image Binarization Algorithm	Time Consumption (ms)
PSO	69.51
GA	535.65
FSA	27.45

means FSA performs well on global solution search because of the "metropolis criteria"; the binary images of it are more similar to the real medium distributions, and the water fraction calculation is much more accurate.

The average time consumptions of the three optimal threshold searching algorithms are listed in Table 6. It can be read from Table 6 that FSA has the minimum time consumption among the three, and GA needs the longest time. Table 5 and Table 6 demonstrate that FSA can not only save time

IEEE *Access*

B. Liu *et al.*: Water Fraction Measurement Method Using Heuristic-Algorithm-Based ECT Images Post-Processing Technology

TABLE 7. The ICC of the images reconstructed by CS-FFPC, LIA, and LBP (experimental).

Medium Distribution	CS-FFPC (%)	LIA (%)	LBP (%)
1	74	59	44
2	81	52	32
3	72	47	37
4	79	49	63
5	61	41	52

consumption, but also obtain an acceptable threshold for image binarization.

To conclude, FSA is the most suitable optimal threshold searching method for water fraction calculation.

IV. EXPERIMENTAL ANALYSIS

For the air-dominated situations, we use thin acrylic tubes (whose inner and outer diameters are 10 mm and 12 mm, respectively) filled with water (relative permittivity is 81) to simulate a static cylindrical aqueous medium, and place it into the designed 12-electrode ECT sensor (whose parameters are illustrated in Table 1). And for the water-dominated situations, set an empty acrylic tube in the center of the sensor, and inject water into the volume between the sensor's and the acrylic tube's wall, simulating annular distribution. The outer diameters of the empty tube for the annular distributions are 18 mm (Fig. 5 (d)) and 16 mm (Fig. 5 (e)), respectively. The spatial positions configurations are shown in Fig. 5.
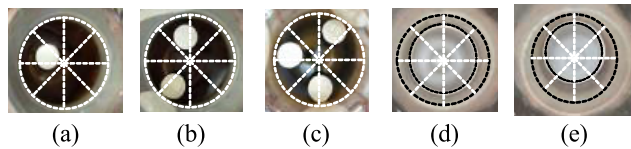
FIGURE 5. ECT gas-water two-phase flow static simulation experiment.

Alternatively change the objects configuration and obtain the capacitance vector of the ECT sensor for each configuration, then use the measured data to validate the proposed method. The reconstructed images are shown in Fig. 6. It can be seen from Fig. 6 that the images reconstructed by CS-FFPC algorithm are much clearer than that of LIA and LBP algorithm. Especially for the annular distribution, it is hard to distinguish the water fraction difference from the images of LBP, and the artifact is serious in the images of LIA.

The ICCs of the images in Fig. 6 are then calculated according to Eq. (21), listed in Table 7. The data in Table 7 quantitatively support the advantage of CS-FFPC algorithm.

Then, apply the FSA-based image binarization algorithm to the reconstructed images; the results are presented in Fig. 7. Obviously, after binary processing, the boundaries of medium distributions are much easier to distinguish, and the water fraction can be calculated then, shown in Table 8.

It can be seen from Table 8 that relative error increases with increasing water fraction. One possible explanation for such
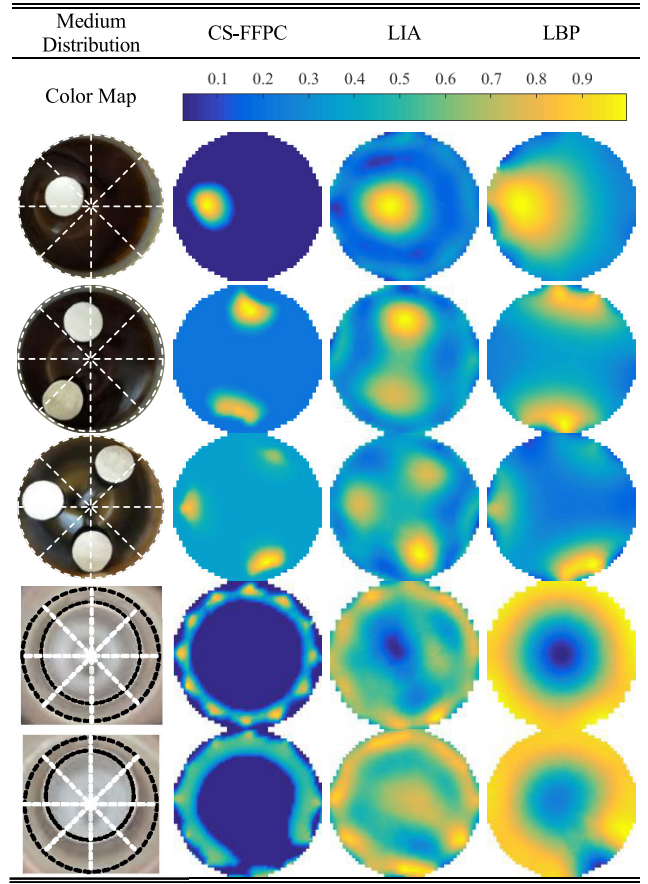
FIGURE 6. The images reconstructed by CS-FFPC, LIA, and LBP (experimental).

TABLE 8. Results of water fraction calculation in static experiment.

Medium Distribution	Algorithm	Real (%)	Calculated (%)	RE (%)
1	CS-FFPC	6.25	6.48	3.68
	LIA		13.23	111.68
	LBP		34.79	456.64
2	CS-FFPC	12.50	11.60	7.20
	LIA		20.14	61.12
	LBP		42.54	240.32
3	CS-FFPC	18.75	20.11	7.25
	LIA		25.86	37.92
	LBP		44.42	136.91
4	CS-FFPC	38.75	33.54	13.45
	LIA		54.84	41.52
	LBP		61.94	80.49
5	CS-FFPC	51.61	44.17	14.42
	LIA		57.87	12.13
	LBP		62.58	21.26

phenomenon is that the volume proportion of the acrylic pipe wall (of the tubes used to simulate the water phase) decreases with the radius.

For the annular distribution number 5, the water fraction calculated by LIA is better than CS-FFPC; however it can be read from Fig. 7 and Table 8 that the binarized images (of
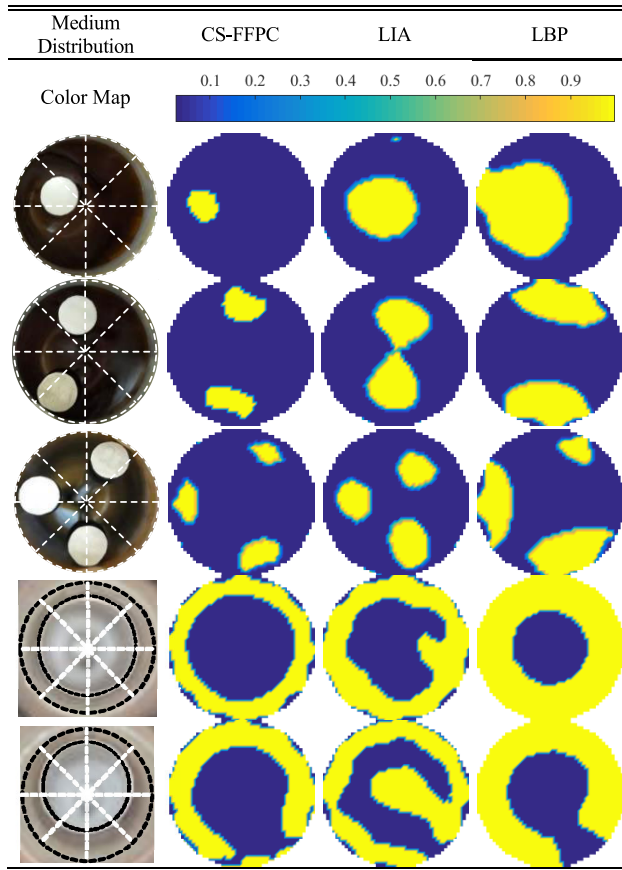
B. Liu *et al.*: Water Fraction Measurement Method Using Heuristic-Algorithm-Based ECT Images Post-Processing Technology

IEEE *Access*

FIGURE 7. Results of the binarized images in static experiment.

TABLE 9. Total time consumption of the three.

Method	Time Consumption (ms)					
	1	2	3	4	5	Avg.
LBP+FSA	38.57	36.17	34.59	34.44	32.89	35.33
LIA+FSA	538.35	429.38	461.16	455.06	443.47	465.48
CS-FFPC+FSA	111.15	111.40	108.46	114.55	105.54	110.22

annular distributions) of LIA and LBP can hardly correctly reflect the real shape of medium, and the calculated water fractions (of annular distributions) are less sensitive to the increment of water volume compared with CS-FFPC. One reason why LIA and LBP perform worse in this application is that there is more artifact in the images reconstructed by LIA and LBP, and the sharpness of their images is far less than CS-FFPC's.

To evaluate the real-time performance of the proposed measurement method, the total time consumed by the whole water fraction calculating procedure is recorded, as shown in Table 9.

The data in Table 9 show that the time consumption for each time of water fraction measurement is slightly larger than the sum of the image reconstruction time (listed in Table 3) and the image binarization time (Table 6). This is because 1) the calculation according to the binary images needs additional time; 2) the run of the designed system's

software needs additional hardware resources, which depends on the programming method. But in general, Table 9 supports that the measurement method of ''CS-FFPC+FSA'' is still practicable to a real-time application.

The performance of the FSA-based binarization using CS-FFPC images is more stable and more accurate than the other two algorithms (LIA and LBP). The relative errors of all medium distribution are lower than 15%, among which the lowest is 3.68%. Table 8 proves the quality of CS-FFPC imaging and FSA binarization. Also, it proves the feasibility of water fraction calculation based on image reconstruction.

V. CONCLUSION

The accurate water fraction measurement for gas-water two-phase flow based on ECT requires reliable and sharpened images of medium distribution within an ECT sensor. To obtain images that suitable for phase fraction calculation, the CS-FFPC image reconstruction algorithm and the FSA-based optimal threshold searching image binarization algorithm are proposed in this paper.

In the simulation section, three image reconstruction algorithms (LIA, LBP, and CS-FFPC) are firstly compared in aspect of image correlation coefficient (ICC), and the CS-FFPC is improved to be the best one among those accordingly; then the three optimal threshold searching methods based on PSO, GA, and FSA respectively are applied to the reconstructed images for water fraction measurement test, whose results validate the advantages of FSA-based image binarization method.

The physical experiments are carried out to further test the performance of the water fraction measurement method that combing the CS-FFPC and FSA optimal threshold image binarization algorithm. The results show that the relative error of the proposed method is below 15%, where the lowest is 3.68%. In conclusion, the proposed method is practical.

In our future work, we plan to optimize the software of the proposed measurement method, and expect to improve the speed of the water fraction measurement.

REFERENCES

[1] G. Lu, L. Peng, B. Zhang, and Y. Liao, ''Preconditioned landweber iteration algorithm for electrical capacitance tomography,'' *Flow Meas. Instrum.*, vol. 16, nos. 2–3, pp. 163–167, Apr. 2005.

[2] F. Dong, Y. B. Xu, L. J. Xu, L. Hua, and X. T. Qiao, ''Application of dual-plane ERT system and cross-correlation technique to measure gas–liquid flows in vertical upward pipe,'' *Flow Meas. Instrum.*, vol. 16, nos. 2–3, pp. 191–197, Apr. 2005.

[3] J. Yu, ''Study on a voidage measurement method based on ERT system and otsu algorithm,'' in *Proc. Chin. Control Decision Conf.*, Jul. 2008, pp. 4939–4942.

[4] W. Wangjiraniran, Y. Motegi, S. Richter, H. Kikura, M. Aritomi, and K. Yamamoto, ''Intrusive effect of wire mesh tomography on gas-liquid flow measurement,'' *J. Nucl. Sci. Technol.*, vol. 40, no. 11, pp. 932–940, Nov. 2003.

[5] W. Wang, ''Voidage measurement of gas-oil two-phase flow,'' *Chin. J. Chem. Eng.*, vol. 15, no. 3, pp. 339–344, Jun. 2007.

[6] X. Li, Z. Huang, B. Wang, and H. Li, ''A new method for the online voidage measurement of the Gas–Oil two-phase flow,'' *IEEE Trans. Instrum. Meas.*, vol. 58, no. 5, pp. 1571–1577, May 2009.

[7] F. R. Moreira da Mota, D. J. Pagano, and M. Enricone Stasiak, ''Water volume fraction estimation in two-phase flow based on electrical capacitance tomography,'' *IEEE Sensors J.*, vol. 18, no. 16, pp. 6822–6835, Aug. 2018.

[8] J. Sun, W. Yang, and W. Tian, ''3D imaging based on fringe effect of an electrical capacitance tomography sensor,'' *Measurement*, vol. 74, pp. 186–199, Oct. 2015.

[9] X. Wang, H. Hu, H. Jia, and K. Tang, ''An AST-ELM method for eliminating the influence of charging phenomenon on ECT,'' *Sensors*, vol. 17, no. 12, p. 2863, Dec. 2017.

[10] D. L. Donoho, ''Compressed sensing,'' *IEEE Trans. Inf. Theory*, vol. 52, no. 4, pp. 1289–1306, Apr. 2006.

[11] C. Xia, C. Su, J. Cao, and P. Li, ''Reconstruction of electrical capacitance tomography images based on fast linearized alternating direction method of multipliers for two-phase flow system,'' *Chin. J. Chem. Eng.*, vol. 24, no. 5, pp. 597–605, May 2016.

[12] L. Zhang and Y. Song, ''Application of gradient projection for sparse reconstruction to compressed sensing for image reconstruction of electrical capacitance tomography,'' *3rd Int. Conf. Electron. Eng. Comput. Sci.*, vol. 2018, pp. 43–49.

[13] J. Ma, J. Xu, Y. Bao, and S. Yu, ''Compressed sensing and its applications: From sparse constraints to low-rank constraints optimization,'' *Signal Process.*, vol. 28, no. 5, pp. 609–623, May 2012.

[14] E. J. Candes, J. Romberg, and T. Tao, ''Robust uncertainty principles: Exact signal reconstruction from highly incomplete frequency information,'' *IEEE Trans. Inf. Theory*, vol. 52, no. 2, pp. 489–509, Feb. 2006.

[15] B. K. Natarajan, ''Sparse approximate solutions to linear systems,'' *SIAM J. Comput.*, vol. 24, no. 2, pp. 227–234, Apr. 1995.

[16] S. S. Chen, D. L. Donoho, and M. A. Saunders, ''Atomic decomposition by basis pursuit,'' *SIAM Rev.*, vol. 43, no. 1, pp. 129–159, Jan. 2001.

[17] L. Zhang, ''Compressed sensing application to electrical capacitance tomography,'' *J. Beijing Univ. Aeronaut. Astronaut.*, vol. 43, no. 11, pp. 139–144, Nov. 2017.

[18] L. Liu, H. Song, and L. Li, ''Research on iteration algorithm based on a fast fixed point in compressed sensing,'' *Comput. Technol. Develop.*, vol. 27, no. 3, pp. 52–56, Mar. 2017.

[19] J. Barzilai and J. M. Borwein, ''Two-point step size gradient methods,'' *IMA J. Numer. Anal.*, vol. 8, no. 1, pp. 141–148, 1988.

[20] M. Loreto and A. Crema, ''Convergence analysis for the modified spectral projected subgradient method,'' *Optim. Lett.*, vol. 9, no. 5, pp. 915–929, Sep. 2014.

[21] G. Shi, ''Advances in theory and application of compressed sensing,'' *ACTA Electronica Sinica*, vol. 37, no. 5, pp. 1070–1081, May 2009.

[22] W. L. Goffe, G. D. Ferrier, and J. Rogers, ''Global optimization of statistical functions with simulated annealing,'' *J. Econometrics*, vol. 60, nos. 1–2, pp. 65–99, Jan. 1994.

[23] H. Szu and R. Hartley, ''Fast simulated annealing,'' *Phys. Lett. A*, vol. 122, nos. 3–4, pp. 157–162, Jun. 1987.

[24] D. Chen, W. Yang, and M. Pan, ''Design of impedance measuring circuits based on phase-sensitive demodulation technique,'' *IEEE Trans. Instrum. Meas.*, vol. 60, no. 4, pp. 1276–1282, Apr. 2011.

[25] K. Tang, H. Hu, L. Li, and X. Wang, ''Composite sensitivity matrix for reducing the influence of medium electrification on electrical capacitance tomography,'' *IEEE Trans. Instrum. Meas.*, vol. 69, no. 4, pp. 1159–1169, Apr. 2020.

BO LIU received the B.Eng. degree from the Harbin Institute of Technology, in 1981. He is currently a Professor and the Vice Dean of the School of Mechanical Engineering, Xi'an Technological University, Xi'an, China. He has authored or coauthored more than 50 academic articles. He has more than ten patents granted. His research interests include special equipment development, advanced sensing, and detection technology.
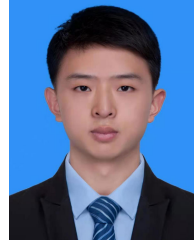
CHENHUI TANG received the B.Eng. degree from Chongqing University, Chongqing, China, in 2017, and the master's degree from Xi'an Jiaotong University, Xi'an, China, in 2020. He is currently working with State Grid Sichuan Electric Power Company Maintenance Company, Chengdu, China. His current research interests include system design of electrical capacitance tomography, multiphase flow measurement in plant, and intelligent instrument design.

KAIHAO TANG received the B.Eng. degree from Chang'an University, Xi'an, China, in 2015. He is currently pursuing the Ph.D. degree in instrument science and technology with the School of Electrical Engineering, Xi'an Jiaotong University, Xi'an. His current research interests include theory and application of electrical tomography, multiphase flow measurement and instrumentation technology, electrical sensing, and digital image and signal processing.

HONGLI HU (Member, IEEE) received the M.Sc. and Ph.D. degrees in electrical engineering and power engineering from Xi'an Jiaotong University, Xi'an, China, in 1991 and 2005, respectively. Since 1991, he has been engaged in teaching and research of measurement and control engineering with the School of Electrical Engineering, Xi'an Jiaotong University, where he is currently affiliated with the Institute for Thermal Engineering. He is also a Professor and a Leader of the Smart Transducer Research Group. He has authored more than 50 research articles. His current research interests include the measurement of multiphase flow, process tomography, and smart transducer systems. He is a member of the Editorial Advisory Board of Flow Measurement and Instrumentation.

• • •